

## Development of interatomic potentials for the complex binary compound $\text{Sb}_2\text{Te}_3$ and the prediction of thermal conductivity

Prabudhya Roy Chowdhury, Tianli Feng, and Xiulin Ruan\*

School of Mechanical Engineering and the Birck Nanotechnology Center, Purdue University, West Lafayette, Indiana 47907-2088, USA



(Received 27 April 2018; revised manuscript received 7 February 2019; published 15 April 2019)

Molecular dynamics (MD) simulation has emerged as a powerful predictive tool to study mechanical and thermal properties of materials, without the requirement for any fitting parameter inputs such as phonon relaxation time. However, the lack of suitable interatomic potentials for many complex materials greatly prohibits effective use of MD simulations to investigate properties of bulk materials and nanostructures. In this paper, we use the method of fitting to an *ab initio* energy surface to develop interatomic potential parameters for the complex binary material antimony telluride, which has important applications in thermoelectric energy generation. Density-functional theory is used to calculate the ground-state electronic structure of the  $\text{Sb}_2\text{Te}_3$  crystal, following which the total energies of a series of artificially distorted lattice configurations are calculated to create the energy surface. A Morse potential functional form is fitted to the energy surface and experimental data, and the parameters are used to calculate the bulk crystal properties and phonon spectra using lattice dynamics. Our parameters are able to reproduce the lattice structure, elastic constants, and acoustic phonon dispersion in good agreement with experimental data. MD simulations are performed using the fitted potential to calculate the thermal conductivity of bulk  $\text{Sb}_2\text{Te}_3$  using the Green-Kubo method. The predicted thermal conductivity shows a  $1/T$  variation in both in-plane and cross-plane directions with the results in the range of experimental measurements. Frequency domain normal mode analysis is used to calculate the modal phonon relaxation times and the accumulation of thermal conductivity with respect to phonon mean free paths. The results show that phonons with mean free paths between 3 and 100 nm contribute to 80% of the total cross-plane thermal conductivity.

DOI: [10.1103/PhysRevB.99.155202](https://doi.org/10.1103/PhysRevB.99.155202)

### I. INTRODUCTION

Experimental discovery of novel materials for various applications needs to be complemented by high-throughput computer simulations of material properties. Due to the availability of modern computer architecture and massively parallel systems, atomic-level methods such as *ab initio* calculations and molecular dynamics (MD) simulations enable us to efficiently predict properties over a variety of system sizes and timescales. In particular, MD simulation has emerged as a powerful tool to predict properties of both bulk materials and nanostructures, due to its capability of simulating large systems ( $\sim 1$  million atoms) for as long as several hundred nanoseconds. Another advantage of MD simulations is that it does not require any fitting parameters as inputs, except suitable interatomic potential parameters to describe the force field.

The development of an appropriate interatomic potential form for a material is a challenging task which involves approximating a complex many-body potential function with generally a simple two-body or three-body form. Although interatomic potentials have been developed for many elemental materials and simple compounds [1], a significant lack of suitable potential parameters is observed for compounds

with complicated crystal structures that can have important applications such as in thermoelectric power generation and photovoltaics. For example,  $\text{Bi}_2\text{Te}_3$  and  $\text{Sb}_2\text{Te}_3$  have been known to exhibit the best bulk thermoelectric properties for more than 50 years; yet interatomic potentials for  $\text{Bi}_2\text{Te}_3$  have only been developed recently [2,3] and are still absent in literature for  $\text{Sb}_2\text{Te}_3$ . Breakthroughs in nanotechnology have enabled experimental demonstrations of even higher thermoelectric performance in  $\text{Bi}_2\text{Te}_3/\text{Sb}_2\text{Te}_3$  nanostructures [4–14]. However, computational studies on such systems are few due to absence of developed potential parameters to describe these materials. The presence of van der Waals interaction and polarization of charges in these compounds makes it even more difficult to develop simple and transferable potential parameters for them.

Traditionally, interatomic potentials are developed by fitting a chosen functional form to reproduce available data for a material. The data used in fitting can be obtained from experimental measurements of bulk crystal properties like lattice constants, bond energies, and elastic and bulk moduli. Such experimental data are generally obtained for the equilibrium state of a material where the atomic interactions are harmonic in nature. However, to accurately predict anharmonic phonon-phonon scattering and heat transfer processes, the interatomic potential must be able to reproduce the anharmonicity in bonds at configurations far from the equilibrium state. Hence, most of these potentials are appropriate for the prediction of

\*ruan@purdue.edu

mechanical properties while not being suited for predicting thermal transport properties. An alternative to using experimental data in the potential fitting process is to generate the required data from *ab initio* calculations. The advantage of this method is that it provides the capability to sample both equilibrium and nonequilibrium states with appropriate weighting parameters chosen according to the purpose of potential development. As a result, these potentials can accurately predict anharmonic vibrational properties such as thermal conductivity. Using this method, Huang and Kaviani developed a three-body potential for bulk  $\text{Bi}_2\text{Te}_3$  and used it in equilibrium MD simulations to predict the phonon thermal conductivity [2], while Qiu and Ruan developed a simpler two-body Morse potential for bulk  $\text{Bi}_2\text{Te}_3$  [3]. The predicted lattice thermal conductivity of the bulk crystal agrees very well with experimental data for both the potentials. As a result, these parameters have been used extensively to study the thermal properties of bulk  $\text{Bi}_2\text{Te}_3$  [2,3,15], thin films [16–19], and nanowires [20,21]. Katcho *et al.* [22] calculated the phonon modes of a  $(\text{Bi}_{1-x}\text{Sb}_x)_2\text{Te}_3$  alloy for any composition  $x$  by using Qiu and Ruan’s  $\text{Bi}_2\text{Te}_3$  potential for  $\text{Sb}_2\text{Te}_3$  with rescaled force constants. The rescaling factor was obtained by fitting to the experimental phonon density of states (PDOS) for bulk  $(\text{Bi}_{1-x}\text{Sb}_x)_2\text{Te}_3$ . However, the bond lengths in bulk  $\text{Sb}_2\text{Te}_3$  are different from that of  $\text{Bi}_2\text{Te}_3$ , and using the same potential parameters for both would result in a strained  $\text{Sb}_2\text{Te}_3$  lattice. More recently, Rohskopf *et al.* [23] used a genetic algorithm-based optimization method to fit a combination of different functional forms of interatomic potentials for Si and Ge. Such modified potentials have been shown to predict the phonon properties well for Si and Ge. Developing simple and accurate potentials for phonon thermal transport in complex compounds is still challenging and an issue of current interest.

In this paper, we describe the procedure of developing a simple two-body Morse potential for the complex binary compound  $\text{Sb}_2\text{Te}_3$  bulk crystal from *ab initio* calculations, and then predict the phonon thermal conductivity using these potential parameters in MD simulations. First, we perform ground-state energies of a large number of atomic configurations of the lattice. The interatomic potential parameters are then fitted to this energy surface along with suitable experimental data such as lattice constants and bulk modulus. The obtained potential parameters are validated using lattice-dynamics calculations by reproducing the bulk crystal structure and harmonic properties. Equilibrium MD simulations are then performed using the Green-Kubo method to predict the lattice thermal conductivity over a temperature range of 200–500 K. Frequency domain normal mode analysis (FD-NMA) is also used to compute the phonon modal relaxation times and the thermal conductivity accumulation with respect to phonon mean-free path.

## II. ELECTRONIC STRUCTURE AND PHONON DISPERSION

Bulk  $\text{Sb}_2\text{Te}_3$  has a tetradymite structure and belongs to the  $D_{3d}^5 (R\bar{3}m)$  space group. The atoms are arranged along the trigonal axis in a quintuple layered structure in the order of Te1-Sb-Te2-Sb-Te1 (Fig. 1). The crystal can be

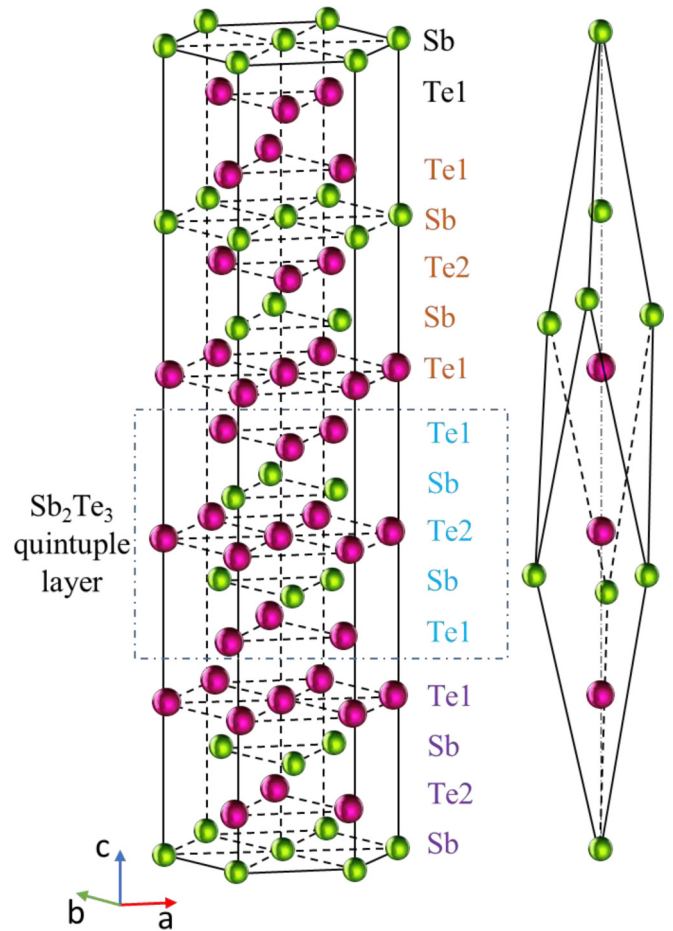


FIG. 1. Quintuple-layered crystal structure of  $\text{Sb}_2\text{Te}_3$  showing rhombohedral (right) and hexagonal (left) unit cells.

described by the primitive rhombohedral unit cell consisting of five atoms. The corresponding lattice parameters are  $a_R = 10.447 \text{ \AA}$ ,  $\theta_R = 23.55^\circ$  with the Sb and Te1 atoms located at  $(\pm u, \pm u, \pm u)$  and  $(\pm v, \pm v, \pm v)$ , respectively, where  $u = 0.3988$  and  $v = 0.2128$  [24]. The more convenient representation is the hexagonal conventional cell (Fig. 1) with lattice parameters  $a = 4.264 \text{ \AA}$  and  $c = 30.458 \text{ \AA}$ . To compute the electronic structure of the bulk crystal, we perform *ab initio* calculations based on the DFT framework, using the projector-augmented wave method as implemented in the VIENNA *Ab initio* SIMULATION PACKAGE (VASP). Electron exchange and correlation is treated using the generalized gradient approximation and the effect of spin-orbital coupling is included, which is necessary to accurately describe heavier elements such as Sb and Te. The cutoff for the plane-wave basis set and the density of the  $k$ -point grid in the Brillouin zone are chosen as 500 eV and  $8 \times 8 \times 8$ , respectively, according to convergence tests. To preserve the layered structure of  $\text{Sb}_2\text{Te}_3$  in which the quintuple layers are held together by weak van der Waals forces of attraction, we also include the DFT-D2 correction method of Grimme [25]. We find, in accordance with previous reports [26], that the van der Waals correction can better reproduce the experimental unit cell parameters. The fully relaxed rhombohedral primitive cell parameters are obtained as  $a_R = 10.597 \text{ \AA}$ ,  $\theta_R = 23.12^\circ$  with

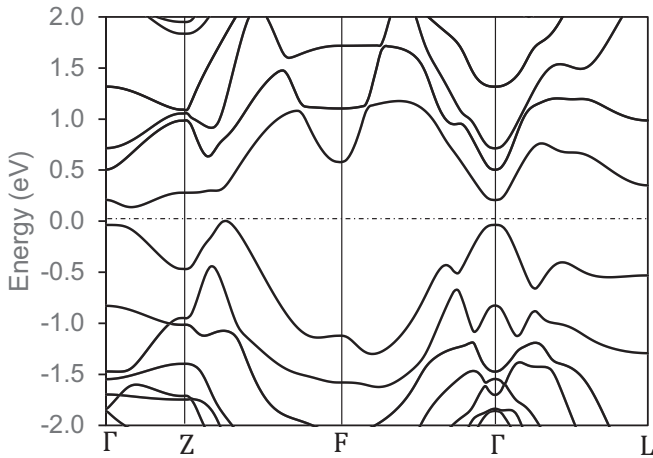


FIG. 2. Electronic band structure of  $\text{Sb}_2\text{Te}_3$  along some high symmetry directions computed using DFT.

the atomic positions at  $u = 0.39712$  and  $v = 0.21370$ , which is in good agreement with previous studies using the DFT-D2 correction [26,27]. The calculated electronic band structure along some high symmetry directions is shown in Fig. 2. Due to the inclusion of spin-orbit coupling, a multivalley band structure is observed, which agrees well with previous studies in literature [28].

To study the phonon properties of bulk  $\text{Sb}_2\text{Te}_3$ , we use the method of finite displacements to calculate the forces and force constants using the PHONOPY code [29] coupled with VASP as the calculator. Forces are calculated on each inequivalent atom in the rhombohedral unit cell to generate the force constants and a  $3 \times 3 \times 3$  supercell is used. Spin-orbital coupling is not included in these calculations since previous reports suggest that the vibrational properties of  $\text{Sb}_2\text{Te}_3$  are not affected significantly by the inclusion of spin-orbital coupling [30]. The obtained PDOS is plotted in Figure 3 and compared to experimental results from inelastic neutron scattering [31]. As seen in the figure, the *ab initio* calculations can successfully reproduce the position and relative strength of the peaks and the overall cutoff range of frequencies with respect to the experimental measurements. The  $A_{1g}$  phonon mode calculated at the Gamma point showed a frequency of 2.15 THz which is very close to the experimental value of 2.07 THz [32]. Since our calculation of the ground-state configuration including the vibrational properties is accurate and consistent with previous reports, it is used to generate the *ab initio* energy surface data for parametrizing the classical interatomic potentials optimized for phonon transport properties.

Once the equilibrium lattice structure is obtained, the different configurations for the *ab initio* energy surface are generated by following a systematic approach: (1) varying the internal atomic coordinates at the equilibrium lattice constant, (2) varying the lattice constant while keeping the internal atomic coordinates (symmetry) fixed, and (3) varying the internal atomic coordinates at different lattice constants. Figure 4 shows a schematic for generating the energy

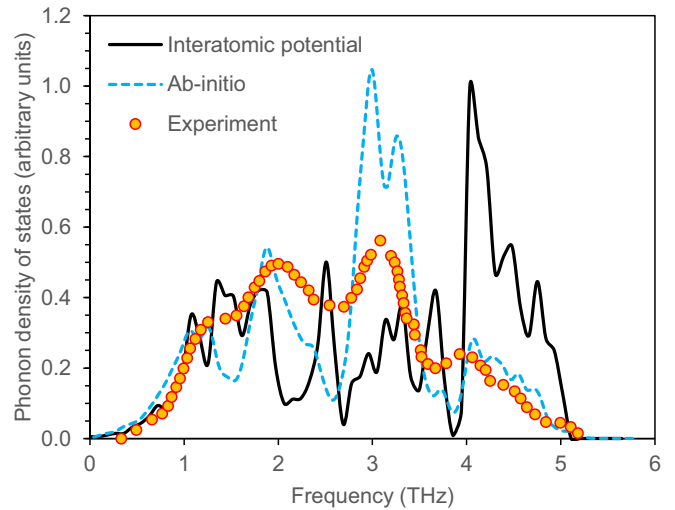


FIG. 3. Phonon density of states of  $\text{Sb}_2\text{Te}_3$  computed from fitted interatomic potential parameters (solid line), *ab initio* calculations (dashed line), and experimental values from Ref. [31] (circles).

surface in this manner using these distorted lattice configurations. Several interatomic potentials have been developed in literature by considering very small atomic displacements from equilibrium, which can represent only the harmonic characteristics of interactions between atoms. Since our aim is to fit potential parameters which can accurately predict thermal conductivity, it is important to consider displacements that can represent the anharmonicity of pairwise interactions in our temperature of interest. To achieve this, the largest displacements from equilibrium positions given to the atoms are around 0.35 Å. This is estimated from the characteristic

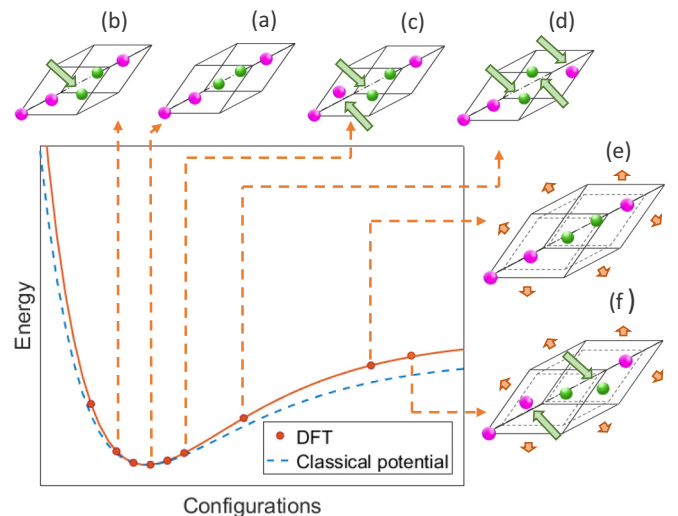


FIG. 4. Schematic showing the generation of the *ab initio* energy surface. The circles represent different configurations used in the energy surface such as the equilibrium configuration (a), displacements of atom(s) at fixed lattice constant [(b)–(d)], variation of lattice constant with atoms fixed at equilibrium positions (e), and displacement of atom(s) at varied lattice constant (f). The dashed line represents the classical interatomic potential fitted to the energy surface.

thermal energy  $k_B T$  at 300 K and displacements of this scale are expected to sample the anharmonicity comprehensively. We have also performed *ab initio* molecular dynamics simulations at 300 K to verify from the trajectories that the atomic displacements are in the same range. As a result, this magnitude of displacement given is sufficient to represent the anharmonic nature of the solid around our temperature of interest. For better performance of the gradient-based fitting process, we artificially build the configurations using these displacements to maintain as much symmetry of the lattice as possible which helps in convergence of the fitting runs.

Apart from varying the internal atomic coordinates, the lattice constant is varied within 1.4% of the equilibrium value, and the atomic positions are varied at different lattice constants. The inclusion of such configurations in the energy surface is necessary to capture the temperature-dependent phonon properties due to thermal expansion. Also, since the bulk modulus is computed from the variation of energy with respect to the volume of the unit cell, the inclusion of these configurations ensure that the fitted parameters are able to reproduce the equilibrium lattice constant and the bulk modulus. Besides fitting to the energy surface, Rohskopf *et al.* [23] proposed fitting to the forces on each atom and the harmonic and third-order interatomic force constants calculated from *ab initio* methods. Forces and force constants are first order and higher order derivatives of the energy surface ( $\frac{\partial E}{\partial r_i}$ ,  $\frac{\partial^2 E}{\partial r_i \partial r_j}$ ,  $\frac{\partial^3 E}{\partial r_i \partial r_j \partial r_k}$ ...), respectively. These are calculated using the method of finite differences from the energy surface data points near the equilibrium configuration. As a result, using force constants should be equivalent to our method of fitting to only the energy surface data, provided the same number of energy surface data points near the equilibrium is used. To generate data points representative of interatomic force constant calculations, we use the open source software ALAMODE [33] to obtain configurations which would be used in force constants calculations, and include these configurations in our *ab initio* energy surface. The total number of configurations we use in fitting are 108, out of which 60 configurations represent variation of internal atomic coordinates at the equilibrium lattice constant, 14 configurations represent variation of the lattice constant with fixed atomic fractional coordinates, 19 configurations represent variation of atomic fractional coordinates at a varied lattice constant, and 15 configurations are made to be representative of force constant calculations.

Above, we have described a hierarchical process of including different configurations at different stages of fitting till the thermal conductivity can be reproduced well. We shall note that currently the methodology does not work in the perfect manner that the fitting converges smoothly as more configurations are added. Due to the complicated nature of the fitting process involving 21 variables, we find that simply adding more configurations to the energy surface does not always generate a better fit. On the contrary, addition of specific structures to the fitting data set sometimes causes the fitting process to diverge, and the relative weights of these configurations in the objective function may need to be adjusted carefully to prevent this from happening. Often, some older configurations need to be removed when new

configurations are added. Another reason that inclusion of more configurations does not always ensure better potential parameters is that the *ab initio* results do not exactly match with the experimental data that are also included as fitting targets. As a result, there needs to be a balance between the number of *ab initio* configurations used and the experimental data included, so that the fitted potential parameters can reproduce both types of observables with good accuracy. Finally, the potential parameters will depend on the purpose the potential is used for and are not unique. For mechanical properties, often only the near-equilibrium configurations need to be considered; for thermal conductivity, anharmonic configurations away from the equilibrium need to receive considerable weight; while for chemical reactions, configurations far away from the equilibrium and near bond-breaking need to be included. This will impact the final fitted parameters since there is no unique way to choose the weighting factors.

### III. CLASSICAL INTERATOMIC POTENTIAL PARAMETERS

Interatomic potentials which can accurately reproduce the quantities of interest are the primary requisite for performing meaningful MD simulations. For complex materials, the choice of the potential functional form is also very important. Many-body potentials may be able to provide a more accurate description of a material along a wider range of simulation conditions, but they involve several parameters and are not very accessible due to their complex forms. On the other hand, most two-body potential forms are simple to implement, computationally less expensive, and can reproduce material properties with good accuracy. For example, the potential parameters developed by Qiu and Ruan for  $\text{Bi}_2\text{Te}_3$  have a simple two-body form which ensures better accessibility, while being able to predict phonon anharmonicity and thermal conductivity very well among other properties [3]. Since no potential parameters exist in literature yet for  $\text{Sb}_2\text{Te}_3$ , we choose to develop two-body interatomic potential parameters which can suitably describe its phonon transport properties.

We use a two-body potential form  $\varphi(r_{ij})$  between atoms  $i$  and  $j$  composed of a short-range interaction term  $\varphi_s(r_{ij})$  and a long-range Coulombic term which can be written as

$$\varphi(r_{ij}) = \varphi_s(r_{ij}) + \frac{q_i q_j}{r_{ij}}, \quad (1)$$

where  $r_{ij}$  is the distance between the atoms  $i$  and  $j$ .  $q_i$  and  $q_j$  are the partial charges on the atoms, which are more appropriate to use for solids like  $\text{Bi}_2\text{Te}_3$  and  $\text{Sb}_2\text{Te}_3$  that have a partially covalent nature. The partial charges used in the potential parameters are 0.30,  $-0.22$ , and  $-0.16$  for Sb, Te1, and Te2 atoms, respectively, which were obtained by allowing the charges to vary during the potential fitting process. In this paper, we use a rigid ion model to fit the atomic charges. Alternatively, a core-shell model might be used to better reproduce the polarization in Sb and Te atoms. However, the increased number of fitting parameters incurred due to this approach makes it very difficult to obtain converged parameters during the parametrization process. The short-range interaction is modeled using the Morse potential form, which is suitable to describe the vibrational properties

TABLE I. Fitted short-range Morse potential parameters for  $\text{Sb}_2\text{Te}_3$ .  $D_e$  is the depth of the potential well,  $a$  is a measure of bond stiffness,  $r$  is the pairwise atomic distance, and  $r_c$  is the cutoff distance.

Type of interaction	$D_e$ (eV)	$a$ ( $1/\text{\AA}$ )	$r_o$ ( $\text{\AA}$ )	$r_c$ ( $\text{\AA}$ )
Sb - Sb	0.089	2.112	4.258	5.5
Te1 - Te1	0.072	1.720	3.795	5.0
Te2 - Te2	0.066	2.639	4.261	5.0
Sb - Te1	1.008	1.292	3.018	4.0
Sb - Te2	0.538	1.166	3.172	4.0
Te1 - Te2	0.750	0.595	4.486	5.5

of solids, including anharmonicity. The functional form is given by

$$\varphi_s(r_{ij}) = D_e[\{1 - e^{-a(r_{ij}-r_o)}\}^2 - 1] \quad (2)$$

Here,  $D_e$  is the depth of the potential well (bond strength),  $a$  is a measure of the width of the well (bond rigidity), and  $r_o$  is the location of the potential well minimum which corresponds to the bond length. As in the case of the two-body potential development of  $\text{Bi}_2\text{Te}_3$  [3], we consider only the nearest-neighbor interactions by carefully choosing the cutoffs for different interactions. This treatment of short-range interactions has been found to be crucial for preserving the complex layered structure of the crystal. The long-range electrostatic potential is computed by the Ewald summation method with a real-space cutoff radius of  $12 \text{\AA}$ .

The potential parameters are fitted to the *ab initio* energy surface using the GENERAL UTILITY LATTICE PROGRAM (GULP) [34], which is designed to handle multivariable optimization problems. The total number of parameters allowed to be fit during the optimization is 21, which includes 18 potential parameters for six different types of interactions, two partial charges, and an energy shift to account for the difference in reference levels for potential energy. The parameters obtained from the fitting process are then used to optimize the crystal structure and calculate bulk properties at the equilibrium configuration. These are compared with experimental data and the process is iterated until the predicted results show good agreement with experimental data. The optimized potential parameters are shown in Table I, along with the cutoff radii  $r_c$ . As in the Morse potential parameters for  $\text{Bi}_2\text{Te}_3$  in Ref. [3], we see that the Te1-Te1 bond has a relatively weak bond energy ( $D_e$ ) along with a high bond stiffness (represented by  $a$ ), which is attributed to the fact that these parameters represent both the weak van der Waals interaction between Te1 atoms of two adjacent quintuple layers (cross plane), as well as the covalent Te1-Te1 interaction within the same layer (in plane). In contrast, the interlayer (cross-plane) Sb-Te1, Sb-Te2, and Te1-Te2 bonds have a higher bond energy and larger anharmonicity which suggests the more ionic nature of these bonds. They also have lower bond stiffness due to which the material elasticity in the cross-plane direction ( $C_{33}$ ) is lower than in the in-plane direction ( $C_{11}$ ). The elastic constants and bulk modulus obtained using the fitted potential parameters are shown in Table II and compared with those

TABLE II. Computation of elastic constants and bulk modulus using fitted potential parameters and comparison with *ab initio* calculations. All quantities are in gigapascals.

Property	<i>Ab initio</i> (this paper)	<i>Ab initio</i> <sup>a</sup>	<i>Ab initio</i> <sup>b</sup>	Classical potential
$C_{11}$	77.5	85.5	83.2	83.8
$C_{12}$	21.9	21.0	21.2	28.1
$C_{13}$	25.5	30.8	46.1	24.7
$C_{14}$	14.3	21.1	-	9.5
$C_{33}$	46.5	50.5	99.7	49.1
$C_{44}$	27.8	37.9	44.6	20.6
$C_{66}$	27.1	-	31.0	27.9
$B$	32.7	42.1	53.2	39.9

<sup>a</sup>Ref. [36].

<sup>b</sup>Ref. [35].

obtained from our own *ab initio* calculations as well as from previous literature [35,36]. It is apparent from these results that the phonon thermal transport in the cross-plane direction is expected to be weaker than that in the in-plane directions.

The fitted potential parameters are also used to calculate the PDOS by computing the dynamical matrix in GULP (Fig. 3). We can see that our classical interatomic potential can successfully reproduce the low-frequency acoustic-phonon portion of the PDOS compared to both *ab initio* calculations and experimental measurements in terms of the position and relative magnitude of the low-frequency peaks. In contrast, the position of the high-frequency optical peak is shifted significantly higher with respect to *ab initio* and experimental data. To further analyze the phonon properties, the phonon dispersion along high-symmetry directions is compared to *ab initio* results and inelastic neutron scattering data [32] in Fig. 5. We can see that the acoustic phonon branches are reproduced in very good agreement with experiment, but the optical branches are overpredicted. These dissimilarities between calculation and experiment can be attributed to using a simple two-body potential form to fit the energy surface, along with the use of a rigid ion model. A more detailed core-shell charge model may be able to improve the optical phonon dispersion by accounting for the charge polarization. In spite of the limitations of our simple potential form, it is able to accurately describe the lattice structure, elastic properties, and dispersion of acoustic phonons. Moreover, simulations of thermal transport in  $\text{Bi}_2\text{Te}_3$  using the Morse potential parameters showed very good agreement with experimental measurements [3], which suggests that the contribution of optical phonons to lattice thermal conductivity is low for these compounds. Since the thermal transport is dominated by the low-frequency acoustic phonons, we can expect that our potential parameters will be able to accurately predict the lattice thermal conductivity of  $\text{Sb}_2\text{Te}_3$ .

#### IV. MOLECULAR DYNAMICS SIMULATIONS OF LATTICE THERMAL CONDUCTIVITY

We use equilibrium molecular dynamics (EMD) to predict the lattice thermal conductivity of  $\text{Sb}_2\text{Te}_3$  in the in-plane and cross-plane directions over a range of temperatures. EMD

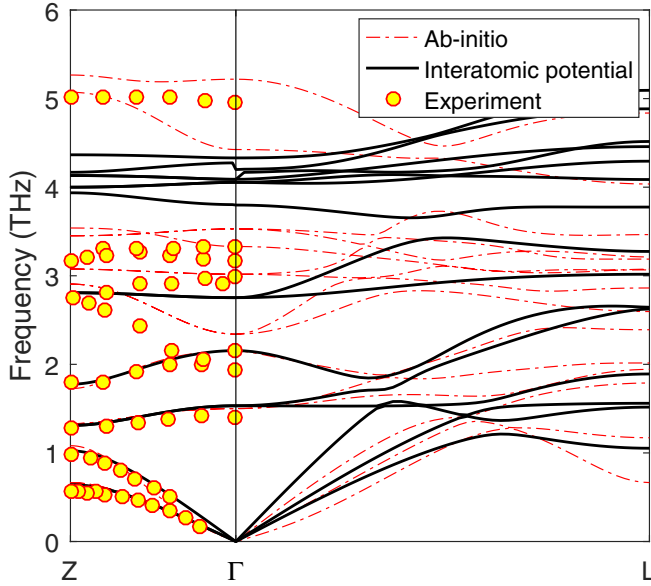


FIG. 5. Phonon dispersion of  $\text{Sb}_2\text{Te}_3$  along some high-symmetry directions computed from *ab initio* calculations (broken line), fitted interatomic potential parameters (solid line) and experimental values from Ref. [32] (circles).

simulations use the Green-Kubo linear-response formulation [37] to predict the thermal transport properties, while the effect of system size has been found to be small due to the application of periodic boundary conditions. Under the Green-Kubo formalism, the phonon thermal conductivity of a system is given by

$$\kappa_{l,\alpha} = \frac{1}{k_B V T^2} \int_0^\infty \langle S_\alpha(0) \cdot S_\alpha(t) \rangle dt, \alpha = x, y, z. \quad (3)$$

Here,  $V$  is the volume of the simulation cell,  $T$  is the absolute temperature in Kelvin,  $S_\alpha(t)$  is the heat current along a particular direction, and  $\langle S_\alpha(0) \cdot S_\alpha(t) \rangle$  represents the heat current autocorrelation function (HCACF). For a pair potential, the heat current is commonly written as

$$\mathbf{S} = \sum_i e_i \mathbf{v}_i + \frac{1}{2} \sum_{i,j} (\mathbf{F}_{ij} \cdot \mathbf{v}_i) \mathbf{r}_{ij}, \quad (4)$$

where  $e_i$  is the energy and  $\mathbf{v}_i$  is the velocity of particle  $i$ , and  $\mathbf{F}_{ij}$  is the force acting between particles  $i$  and  $j$  separated by  $\mathbf{r}_{ij}$ . The integral in Eq. (3) is in practice carried out over a finite time interval which needs to be decided appropriately based on the longest phonon lifetimes existing in the material.

We performed MD simulations of bulk  $\text{Sb}_2\text{Te}_3$  on a system consisting of  $6 \times 6 \times 2$  hexagonal unit cells with a total of 1080 atoms. Convergence tests with larger system sizes show negligible size effects. The equations of motion are integrated using the Verlet algorithm with a time step of 0.25 fs, which is sufficient to resolve the highest frequency phonon mode calculated from lattice dynamics, while the Nose-Hoover thermostat is used to regulate system temperature. Initially, the bulk lattice structure is equilibrated under constant temperature and pressure (NPT) for 250 ps to minimize the stress on the system, after which it is switched to a constant energy and volume (NVE) ensemble and run for another 250 ps to

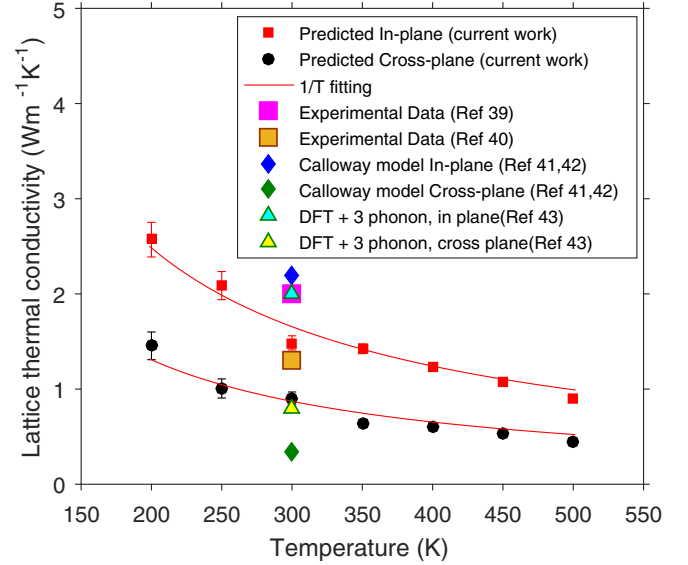


FIG. 6. MD predicted thermal conductivity in in-plane and cross-plane directions and 1/T fitting compared with experimental data (Refs. [39,40]), calculations using a modified Calloway model (Refs. [41,42]), and BTE + 3 phonon calculations (Ref. [43]).

observe conservation of energy. Following this step, the heat current data is obtained for 20 ns to compute the HCACF, with a sampling interval of 10 time steps. MD simulations are performed over a temperature range of 200 K to 500 K with an interval of 50 K.

To minimize statistical fluctuations, we perform runs for 10 independent ensembles at every temperature. The uncertainty associated with calculation of thermal conductivity from equilibrium MD simulations has recently been quantified by Wang *et al.* [38] who correlated the standard deviation  $\sigma_\kappa$  of the predicted thermal conductivity about the average  $\kappa_{\text{ave}}$ , with the total simulation time  $t_{\text{total}}$ , HCACF correlation time length  $t_{\text{corr}}$ , and number of independent runs  $N$  as

$$\frac{\sigma_\kappa}{\kappa_{\text{ave}}} = 2 \left( \frac{N \times t_{\text{total}}}{t_{\text{corr}}} \right)^{-0.5} \quad (5)$$

Based on their suggestion, we compared the thermal conductivity from MD simulations performed for the system at 300 K with a total time of 2 ns and 20 ns and a fixed correlation time of 125 ps. Our results indeed show that the spread in thermal conductivity values from different runs reduces significantly with increasing total simulation time, which is expected since time averaging in MD simulations is equivalent to ensemble averaging.

The variation of lattice thermal conductivity  $\kappa_l$  in both in-plane and cross-plane directions with temperature is shown in Fig. 6, along with the 1/T fitting. The error bars for each data point have been obtained using Eq. (5). Both the in-plane and the cross-plane thermal conductivities generally follow a 1/T curve which indicates the dominance of Umklapp scattering. Experimental measurements of thermal conductivity of bulk  $\text{Sb}_2\text{Te}_3$  in literature have large discrepancies among themselves. This may be due to the fact that the values reported often do not separate either the contributions from electronic and lattice contributions, or the in-plane and

cross-plane anisotropy which is high for a layered material such as  $\text{Sb}_2\text{Te}_3$ . The reported values for total thermal conductivity vary widely from 2–5  $\text{Wm}^{-1}\text{K}^{-1}$  [39,40,44–48] while the lattice thermal conductivity is generally estimated at around 1.3–2.5  $\text{Wm}^{-1}\text{K}^{-1}$  [39,40,47,48]. The theoretical lattice thermal conductivity has been calculated using the modified Callaway model as  $\kappa_{\parallel} = 2.2 \text{ Wm}^{-1}\text{K}^{-1}$  and  $\kappa_{\perp} = 0.34 \text{ Wm}^{-1}\text{K}^{-1}$  [41,42]. Campi *et al.* [43] predicted the thermal conductivity of  $\text{Sb}_2\text{Te}_3$  from first principles by solving the Boltzmann transport equation. The phonon-phonon scattering was derived by calculating the anharmonic force constants using the framework of density functional perturbation theory. The in-plane thermal conductivity at 300 K obtained in their work is 2.0  $\text{Wm}^{-1}\text{K}^{-1}$ , which is higher than the results we observe in our calculations, while the cross-plane thermal conductivity obtained is 0.8  $\text{Wm}^{-1}\text{K}^{-1}$ , which agrees well with our results. The higher in-plane conductivity may be due to the fact that the authors in Ref. [43] have included only three-phonon scattering in their computations, while our MD treatment inherently includes higher order processes such as four-phonon scattering, which may be important [49–51]. Besides, the inaccuracy of the potential to reproduce the optical phonon dispersion may also contribute to the observed discrepancy.

## V. PHONON MODAL RELAXATION TIME AND THERMAL CONDUCTIVITY ACCUMULATION

We also calculate the contribution of different phonon modes to the total cross-plane lattice thermal conductivity using FD-NMA. The total thermal conductivity can be obtained as the sum of the modewise thermal conductivities  $k_j$  of all phonon modes in the first Brillouin zone,

$$\kappa_z = \sum_j \kappa_j = \frac{1}{(2\pi)^3} \sum_{\nu} \int (\mathbf{v}_{\lambda} \cdot \hat{\mathbf{z}})^2 c_{\lambda} \tau_{\lambda} d\mathbf{k}, \quad (6)$$

where  $z$  is the cross-plane direction,  $\lambda$  represents the phonon mode  $(\mathbf{k}, \nu)$  with  $\mathbf{k}$  being the wave vector and  $\nu$  the polarization branch,  $c_{\lambda}$  is the phonon mode specific heat,  $\tau_{\lambda}$  is the relaxation time,  $\mathbf{v}_{\lambda}$  is the group velocity, and the summation over the Brillouin zone is converted to the continuous integral form using  $\sum_{\mathbf{k}} = V/(2\pi)^3 \int d\mathbf{k}$ . The specific heat per phonon mode is given by  $c_{\lambda} = \hbar\omega_{\lambda} \partial n_{\lambda}^0 / \partial T = k_B x^2 e^x / (e^x - 1)^2$ , where  $x = \hbar\omega/k_B T$ , and the phonon occupation number  $n_{\lambda}^0 = 1/(e^x - 1)$  according to the Bose-Einstein distribution. The phonon group velocity is given by the gradient of the phonon dispersion,  $v = d\omega/dk$ , where  $\omega$  is the phonon angular frequency.

The FD-NMA method was initially developed by Wang *et al.* [52] and later extended by Shiomi and Maruyama [53], de Koker [54], Thomas *et al.* [55], and Feng *et al.* [56] According to lattice dynamics, the vibrations of atoms in real space can be mapped to the time-dependent normal mode coordinates:

$$q_{\lambda}(t) = \sum_{\alpha}^3 \sum_b^n \sum_l^{N_c} \sqrt{\frac{m_b}{N_c}} u_{\alpha}^{l,b}(t) e_{b,\alpha}^{\lambda*} \exp[i\mathbf{k} \cdot \mathbf{r}_0^l]. \quad (7)$$

Here,  $u_{\alpha}^{l,b}(t)$  is the  $\alpha$  component of displacement of the  $b$ th basis atom with mass  $m_b$  in the  $l$ th unit cell from equilibrium

position,  $e_{b,\alpha}^{\lambda*}$  is the complex conjugate of the eigenvector component of the phonon mode  $\lambda$ ,  $n$  is the total number of basis atoms in a unit cell, and  $N_c$  is the total number of unit cells. In FD-NMA, the total spectral energy density (SED) is calculated for each  $\mathbf{k}$ -point from the sum of the SED's of all phonon branches,

$$\Phi(\mathbf{k}, \omega) = \sum_{\nu}^{3n} \Phi_{\nu}(\mathbf{k}, \omega) = \sum_{\nu}^{3n} |\dot{q}_{\mathbf{k},\nu}(\omega)|^2, \quad (8)$$

where

$$\begin{aligned} \Phi_{\nu}(\mathbf{k}, \omega) &= |\dot{q}_{\mathbf{k},\nu}(\omega)|^2 = \left| \int_0^{\infty} \dot{q}_{\mathbf{k},\nu}(t) e^{-i\omega t} dt \right|^2 \\ &= \frac{C_{\mathbf{k},\nu}}{(\omega - \omega_{\mathbf{k},\nu}^A)^2 + \Gamma_{\mathbf{k},\nu}^2}. \end{aligned} \quad (9)$$

Here,  $\Phi_{\nu}(\mathbf{k}, \omega)$  is the Fourier transform of the time derivative of  $q_{\mathbf{k},\nu}(t)$  and  $C_{\mathbf{k},\nu}$  is a constant of fitting related to the normal mode vibrational amplitude  $q_{\mathbf{k},\nu,0}$ . By fitting the SED function at each  $\mathbf{k}$ -point to  $3n$  Lorentzian forms, we can extract the anharmonic phonon frequency  $\omega$  for each phonon mode. The phonon relaxation time  $\tau_{\lambda}$  is also obtained from the full width at half maximum of the fitted curve as  $\tau_{\lambda} = 1/2\Gamma_{\mathbf{k},\nu}$ . It is to be noted here that due to the finite size and periodicity requirements of the MD domain, not all  $\mathbf{k}$ -vectors in the Brillouin zone can be sampled. Only those  $\mathbf{k}$ -points in the first Brillouin zone satisfying the condition  $e^{-i\mathbf{k} \cdot \mathbf{r}} = 1$  can be resolved in the MD normal mode analysis, where  $\mathbf{r} = \sum_{i=1}^3 n_i \mathbf{A}_i$  and  $\mathbf{A}_i$  is the length vector of the simulation domain in direction  $i$ .

We perform FD-NMA on a  $12 \times 12 \times 12$  rhombohedral cell with five basis atoms, and a  $12 \times 12 \times 12$   $\mathbf{k}$ -point grid uniformly sampling the first Brillouin zone. The rhombohedral primitive cell is used since the number of phonon dispersion branches in this case is much less than that obtained using the hexagonal cell, which makes the SED analysis simpler. The system is first relaxed under an NPT ensemble at 300 K for 200 ps and further under an NVE ensemble for 200 ps. Following this, the system is run in an NVE ensemble to compute the normal mode amplitudes from the MD trajectories at an interval of 10 fs, which is shorter than the shortest phonon time period. The anharmonic phonon dispersion computed from NMA along the  $\Gamma - Z$  direction is shown in Fig. 7(a) along with the harmonic phonon dispersion computed from GULP for comparison, and also the quasiharmonic dispersion computed with the lattice constant at 300 K. It is seen that there is noticeable softening of the phonon modes at finite temperature, which proves that our developed interatomic potential can capture the anharmonicity of the material. The quasiharmonic results are very similar to the fully anharmonic results, indicating that the frequency shift is mainly due to the lattice expansion. The phonon relaxation times predicted by FD-NMA along the  $\Gamma - Z$  direction are shown in Fig. 7(b), where it can be seen that the phonon lifetime decreases with increasing phonon frequency. The lifetimes of acoustic phonons below 1 THz are very well fitted with a  $\tau \propto f^{-2}$  form [Fig. 7(c)], which is generally the power law expression used in many works for calculating the thermal conductivity analytically. The lifetime of the  $A_{1g}$  phonon mode is predicted by the FD-NMA to be 4.5 ps,

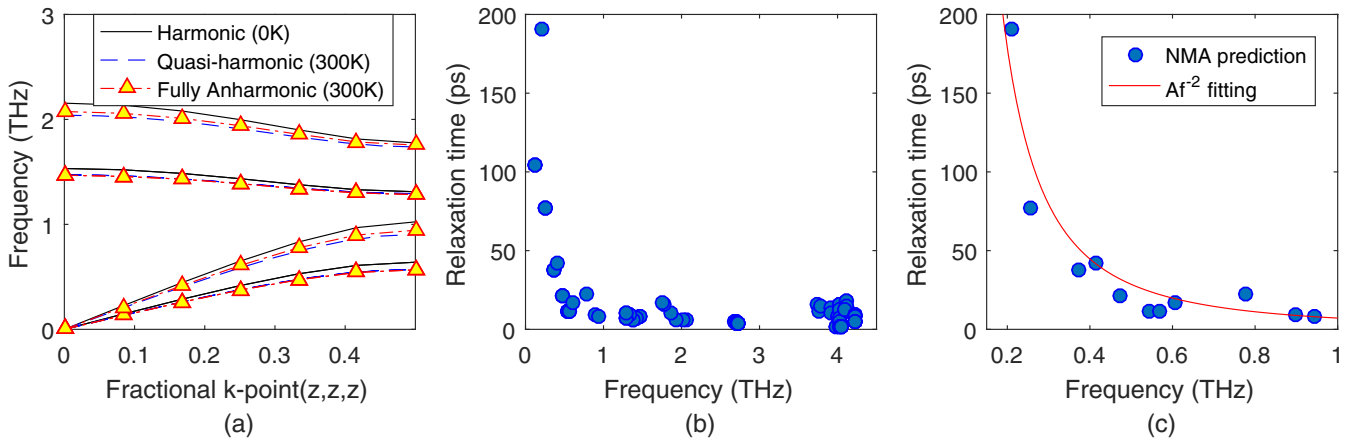


FIG. 7. (a) Anharmonic phonon dispersion at 300 K from NMA (triangles and broken lines), quasi-harmonic phonon dispersion (300 K) from LD (dashed lines), and harmonic phonon dispersion (0 K) from LD (solid lines) along the  $\Gamma - Z$  direction. (b) Relaxation times of phonons along the  $\Gamma - Z$  direction. (c) Relaxation times of low-frequency acoustic phonons along  $\Gamma - Z$ , along with  $f^{-2}$  fitting.

compared to the experimental value of 3.4 ps obtained from time-resolved reflectivity measurements using femtosecond pulses [57]. The overall range of phonon lifetimes is also similar to the phonon lifetimes calculated for  $\text{Bi}_2\text{Te}_3$  using time-domain normal mode analysis by Wang *et al.* [58].

The phonon relaxation times obtained using FD-NMA and the group velocities are used in Eq. (6) to calculate the thermal conductivity of each phonon mode as well as the total thermal conductivity. Obtaining a converged sum from Eq. (6) requires proper discretization of the Brillouin zone to ensure we capture all important phonon modes. Due to the finite size of the MD simulation domain, the contribution of phonon modes with very long wavelengths is absent; however, the density of states for these low frequency modes is low. We have performed calculations for an  $8 \times 8 \times 8$  simulation domain with an  $8 \times 8 \times 8$  k-point grid to test the size effect. The results for phonon lifetimes and total thermal conductivity

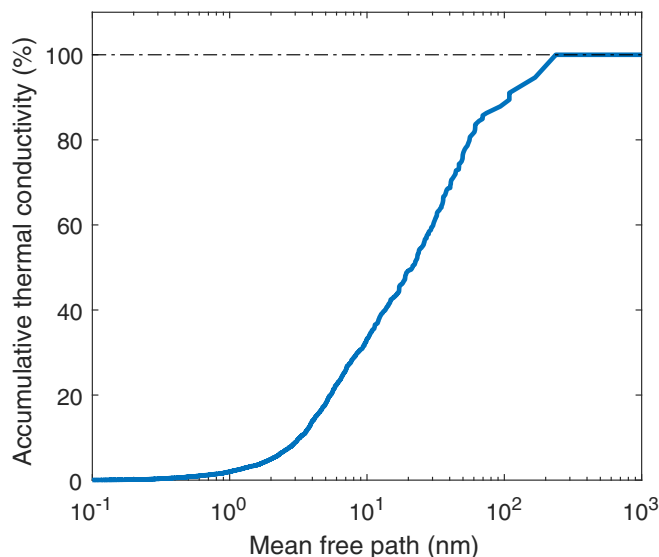


FIG. 8. Accumulated thermal conductivity (%) with respect to phonon mean-free path.

are similar to the  $12 \times 12 \times 12$  cell system, which suggests that our k-grid resolution is able to ensure a converged sum. The total cross-plane thermal conductivity obtained from FD-NMA is 0.92 W/mK, which agrees very well with the EMD value of 0.89 W/mK. The difference in the two results can be attributed to process of fitting the Lorentzian form to a large number of phonon modes, particularly for the higher frequency peaks which are often clustered together and difficult to isolate. The accumulation of thermal conductivity in the cross-plane direction with respect to phonon mean-free path is shown in Fig. 8, where the mean-free paths along the cross-plane direction can also be obtained using the relation  $\lambda = (v \cdot \hat{z})$ . The results in Fig. 8 show that phonons with mean-free paths between 3 and 100 nm contribute to around 80% of the total cross-plane thermal conductivity. The contribution of acoustic phonons to total thermal conductivity is 80% while the contribution of optical phonons is 20%, compared to a 35% contribution of optical phonons calculated by Campi *et al.* [43] from first principles.

## VI. CONCLUSIONS

In summary, we have used DFT to calculate the electronic band structure of bulk  $\text{Sb}_2\text{Te}_3$  and the energies of different representative configurations away from equilibrium. We then fit a two-body Morse interatomic potential form to the energy surface and experimentally observed crystal properties like lattice constants and bulk modulus. The fitted potential form can reproduce the lattice structure and acoustic phonon dispersion of the crystal in very good agreement with experiment, indicating that our developed potential is suitable to describe phonon thermal transport in the material. MD simulations using the Green-Kubo linear response framework have then been performed using this interatomic potential, and the lattice thermal conductivity in the in-plane and cross-plane directions have been predicted over a range of temperature from 200–500 K. The in-plane thermal conductivity was found to vary from 0.9 – 2.6  $\text{Wm}^{-1}\text{K}^{-1}$ , while the cross-plane thermal conductivity was found to vary from 0.4 – 1.5  $\text{Wm}^{-1}\text{K}^{-1}$  as the temperature is decreased from 500 K to 200 K. The results

at room temperature agree well with the range of experimental values found in literature. The nature of phonon transport in  $\text{Sb}_2\text{Te}_3$  is found to be extremely similar to that in  $\text{Bi}_2\text{Te}_3$  as expected, with the cross-plane thermal conductivity much lower than the in-plane one due to the weak nature of the van der Waals bonds in the interlayer direction. The modal decomposition of the cross-plane thermal conductivity is also performed using FD-NMA. The anharmonic phonon dispersion along the  $\Gamma - Z$  cross-plane direction shows softening of phonon frequencies, while the acoustic phonons are found to be approximated well by a  $f^{-2}$  fitting. In addition to being

able to predict the thermal conductivity of bulk  $\text{Sb}_2\text{Te}_3$ , this potential may be applied to the study of thermal transport in  $\text{Bi}_2\text{Te}_3$ - $\text{Sb}_2\text{Te}_3$  alloys and nanostructures, which is the scope of future work.

#### ACKNOWLEDGMENTS

This work was supported by the Defense Advanced Research Projects Agency (Award No. HR0011-15-2-0037) and the School of Mechanical Engineering, Purdue University. Simulations have been performed at the Rosen Center for Advanced Computing at Purdue University.

- 
- [1] NIST Interatomic Potentials Repository: <http://www.ctcms.nist.gov/potentials>.
- [2] B.-L. Huang and M. Kaviani, *Phys. Rev. B* **77**, 125209 (2008).
- [3] B. Qiu and X. Ruan, *Phys. Rev. B* **80**, 165203 (2009).
- [4] R. Venkatasubramanian, E. Siivola, T. Colpitts, and B. O'Quinn, *Nature* **413**, 597 (2001).
- [5] R. Venkatasubramanian, *Phys. Rev. B* **61**, 3091 (2000).
- [6] X. Tang, W. Xie, H. Li, W. Zhao, Q. Zhang, and M. Niino, *Appl. Phys. Lett.* **90**, 012102 (2007).
- [7] B. Poudel, Q. Hao, Y. Ma, Y. Lan, A. Minnich, B. Yu, X. Yan, D. Wang, A. Muto, D. Vashaee, X. Chen, J. Liu, M. S. Dresselhaus, G. Chen, and Z. Ren, *Science* **320**, 634 (2008).
- [8] Y. Q. Cao, X. B. Zhao, T. J. Zhu, X. B. Zhang, and J. P. Tu, *Appl. Phys. Lett.* **92**, 143106 (2008).
- [9] J. Zhou, C. Jin, J. H. Seol, X. Li, and L. Shi, *Appl. Phys. Lett.* **87**, 133109 (2005).
- [10] A. Mavrokefalos, A. L. Moore, M. T. Pettes, L. Shi, W. Wang, and X. Li, *J. Appl. Phys.* **105**, 104318 (2009).
- [11] H. Fang, T. Feng, H. Yang, X. Ruan, and Y. Wu, *Nano Lett.* **13**, 2058 (2013).
- [12] L. Li, S. Xu, and G. Li, *Energy Technol.* **3**, 825 (2015).
- [13] M. B. Khedim, L. Cagnon, V. Serradeil, T. Fournier, and D. Bourgault, *Mater. Today: Proc.* **2**, 602 (2015), 12th European Conference on Thermoelectrics.
- [14] I. Ng, K. Kok, C. C. A. Rahman, T. Choo, and N. Saidin, *Mater. Today: Proc.* **3**, 533 (2016), Advances in Functional Materials (Conference 2015).
- [15] Y. Tong, F. Yi, L. Liu, P. Zhai, and Q. Zhang, *Comput. Mater. Sci.* **48**, 343 (2010).
- [16] C. Shao and H. Bao, *Sci. Rep.* **6**, 27492 (2016).
- [17] Y. Tong, F. Yi, L. Liu, P. Zhai, and Q. Zhang, *Physica B (Amsterdam)* **405**, 3190 (2010).
- [18] B. Qiu and X. Ruan, *Appl. Phys. Lett.* **97**, 183107 (2010).
- [19] J. Zhang, H. J. Liu, L. Cheng, J. Wei, J. Shi, X. F. Tang, and C. Uher, *J. Appl. Phys.* **116**, 023706 (2014).
- [20] Y. Tong, F. J. Yi, L. S. Liu, and Q. J. Zhang, *J. Electron. Mater.* **39**, 1730 (2010).
- [21] B. Qiu, L. Sun, and X. Ruan, *Phys. Rev. B* **83**, 035312 (2011).
- [22] N. A. Katcho, N. Mingo, and D. A. Broido, *Phys. Rev. B* **85**, 115208 (2012).
- [23] A. Rohskopf, H. R. Seyf, K. Gordiz, T. Tadano, and A. Henry, *npj Comput. Mater.* **3**, 27 (2017).
- [24] T. L. Anderson and H. B. Krause, *Acta Crystallogr. Sect. B* **30**, 1307 (1974).
- [25] S. Grimme, *J. Comput. Chem.* **27**, 1787 (2006).
- [26] R. P. Stoffel, V. L. Deringer, R. E. Simon, R. P. Hermann, and R. Dronskowski, *J. Phys.: Condens. Matter* **27**, 085402 (2015).
- [27] K. Zhao, Y. Wang, Y. Sui, C. Xin, X. Wang, Y. Wang, Z. Liu, and B. Li, *Phys. Status Solidi – Rapid Res. Lett.* **9**, 379 (2015).
- [28] T. Thonhauser, T. J. Scheidemantel, J. O. Sofo, J. V. Badding, and G. D. Mahan, *Phys. Rev. B* **68**, 085201 (2003).
- [29] A. Togo and I. Tanaka, *Scr. Mater.* **108**, 1 (2015).
- [30] V. Chis, I. Y. Sklyadneva, K. A. Kokh, V. A. Volodin, O. E. Tereshchenko, and E. V. Chulkov, *Phys. Rev. B* **86**, 174304 (2012).
- [31] H. Rauh, R. Geick, H. Kohler, N. Nucker, and N. Lehner, *J. Phys. C* **14**, 2705 (1981).
- [32] O. Madelung, U. Rössler, and M. Schulz (eds.), in *Non-Tetrahedrally Bonded Elements and Binary Compounds I*, Landolt-Börnstein - Group III Condensed Matter, Vol. 41C (Springer-Verlag, Heidelberg, 1998), pp. 1–5.
- [33] T. Tadano, Y. Gohda, and S. Tsuneyuki, *J. Phys.: Condens. Matter* **26**, 225402 (2014).
- [34] J. D. Gale, *J. Chem. Soc., Faraday Trans.* **93**, 629 (1997).
- [35] Q. Lu, H.-Y. Zhang, Y. Cheng, X.-R. Chen, and G.-F. Ji, *Chin. Phys. B* **25**, 026401 (2016).
- [36] H. Koc, A. M. Mamedov, and E. Ozbay, in *2013 Joint IEEE International Symposium on Applications of Ferroelectric and Workshop on Piezoresponse Force Microscopy (ISAF/PFM)* (2013), pp. 41–44.
- [37] R. Kubo, M. Toda, and N. Hashitsume, *Statistical Physics II: Nonequilibrium Statistical Mechanics*, Vol. 31 (Springer Science & Business Media, Berlin, 2012).
- [38] Z. Wang, S. Safarkhani, G. Lin, and X. Ruan, *Int. J. Heat Mass Transf.* **112**, 267 (2017).
- [39] L. Testardi, J. Bierly, and F. Donahoe, *J. Phys. Chem. Solids* **23**, 1209 (1962).
- [40] L. E. Shelimova, O. G. Karpinskii, P. P. Konstantinov, M. A. Kretova, E. S. Avilov, and V. S. Zemskov, *Inorg. Mater.* **37**, 342 (2001).
- [41] D. M. Rowe, *CRC Handbook of Thermoelectrics* (CRC Press Boca Raton, Florida, 1995).
- [42] W.-Y. Lee, N.-W. Park, S.-G. Yoon, and S.-K. Lee, *J. Nanosci. Nanotechnol.* **16**, 7567 (2016).

- [43] D. Campi, L. Paulatto, G. Fugallo, F. Mauri, and M. Bernasconi, *Phys. Rev. B* **95**, 024311 (2017).
- [44] T. Harman, B. Paris, S. Miller, and H. Goering, *J. Phys. Chem. Solids* **2**, 181 (1957).
- [45] C. H. Champness, P. T. Chiang, and P. Parekh, *Can. J. Phys.* **43**, 653 (1965).
- [46] Y. Touloukian, R. Powell, C. Ho, P. Klemens, THERMOPHYSICAL, and E. P. I. A. C. L. IN., *Thermophysical Properties of Matter*, TPRC Data Series, Vol. 1., Thermal Conductivity—Metallic Elements and Alloys (Defense Technical Information Center, New York, Washington, 1970).
- [47] K. Yokota and S. Katayama, *Jpn. J. Appl. Phys.* **12**, 1205 (1973).
- [48] R. Lan, R. Endo, M. Kuwahara, Y. Kobayashi, and M. Susa, *Jpn. J. Appl. Phys.* **49**, 078003 (2010).
- [49] T. Feng and X. Ruan, *Phys. Rev. B* **93**, 045202 (2016).
- [50] T. Feng, L. Lindsay, and X. Ruan, *Phys. Rev. B* **96**, 161201(R) (2017).
- [51] T. Feng and X. Ruan, *Phys. Rev. B* **97**, 045202 (2018).
- [52] C. Z. Wang, C. T. Chan, and K. M. Ho, *Phys. Rev. B* **40**, 3390 (1989).
- [53] J. Shiomi and S. Maruyama, *Phys. Rev. B* **73**, 205420 (2006).
- [54] N. de Koker, *Phys. Rev. Lett.* **103**, 125902 (2009).
- [55] J. A. Thomas, J. E. Turney, R. M. Iutzi, C. H. Amon, and A. J. H. McGaughey, *Phys. Rev. B* **81**, 081411(R) (2010).
- [56] T. Feng, B. Qiu, and X. Ruan, *J. Appl. Phys.* **117**, 195102 (2015).
- [57] Y. Wang, X. Xu, and R. Venkatasubramanian, *Appl. Phys. Lett.* **93**, 113114 (2008).
- [58] Y. Wang, B. Qiu, A. J. McGaughey, X. Ruan, and X. Xu, *J. Heat Transfer* **135**, 091102 (2013).